Local administration of porcine immunomodulatory, chemotactic and angiogenic extracellular vesicles using engineered cardiac scaffolds for myocardial infarction

Marta Monguió-Tortajada [a,b,c,d,1], Cristina Prat-Vidal [a,d,e,1], Miriam Moron-Font [b], Marta Clos-Sansalvador [b,c], Alexandra Calle [f], Paloma Gastelurrutia [a,d,e], Adriana Cserkoova [a], Anna Morancho [g], Miguel Ángel Ramírez [f], Anna Rosell [g], Antoni Bayes-Genis [a,d,h,i], Carolina Gálvez-Montón [a,d,2,***], Francesc E. Borràs [b,c,j,2,*], Santiago Roura [a,d,k,2,**]

[a] ICREC Research Program, Health Science Research Institute Germans Trias i Pujol (IGTP), Can Ruti Campus, Badalona, Spain
[b] REMAR-IVECAT Group, Health Science Research Institute Germans Trias i Pujol (IGTP), Can Ruti Campus, Badalona, Spain
[c] Department of Cell Biology, Physiology and Immunology, Universitat Autònoma de Barcelona (UAB), Bellaterra, Spain
[d] CIBERCV, Instituto de Salud Carlos III, Madrid, Spain
[e] Institut d'Investigació Biomèdica de Bellvitge-IDIBELL, L'Hospitalet de Llobregat, Spain
[f] Departamento de Reproducción Animal, Instituto Nacional de Investigación y Tecnología Agraria y Alimentaria (INIA), Madrid, Spain
[g] Neurovascular Research Laboratory, Vall d'Hebron Research Institute (VHIR), UAB, Barcelona, Spain
[h] Cardiology Service, Germans Trias i Pujol University Hospital, Badalona, Spain
[i] Department of Medicine, UAB, Barcelona, Spain
[j] Nephrology Service, Germans Trias i Pujol University Hospital, Badalona, Spain
[k] Faculty of Medicine, University of Vic-Central University of Catalonia (UVic-UCC), Vic, Barcelona, 08500, Spain

ARTICLE INFO

ABSTRACT

The administration of extracellular vesicles (EV) from mesenchymal stromal cells (MSC) is a promising cell-free nanotherapy for tissue repair after myocardial infarction (MI). However, the optimal EV delivery strategy remains undetermined. Here, we designed a novel MSC-EV delivery, using 3D scaffolds engineered from decellularised cardiac tissue as a cell-free product for cardiac repair. EV from porcine cardiac adipose tissue-derived MSC (cATMSC) were purified by size exclusion chromatography (SEC), functionally analysed and loaded to scaffolds. cATMSC-EV markedly reduced polyclonal proliferation and pro-inflammatory cytokines production (IFNγ, TNFα, IL12p40) of allogeneic PBMC. Moreover, cATMSC-EV recruited outgrowth endothelial cells (OEC) and allogeneic MSC, and promoted angiogenesis. Fluorescently labelled cATMSC-EV were mixed with peptide hydrogel, and were successfully retained in decellularised scaffolds. Then, cATMSC-EV-embedded pericardial scaffolds were administered *in vivo* over the ischemic myocardium in a pig model of MI. Six days from implantation, the engineered scaffold efficiently integrated into the post-infarcted myocardium. cATMSC-EV were detected within the construct and MI core, and promoted an increase in vascular density and reduction in macrophage and T cell infiltration within the damaged myocardium. The confined administration of multi-functional MSC-EV within an engineered pericardial scaffold ensures local EV dosage and release, and generates a vascularised bioactive niche for cell recruitment, engraftment and modulation of short-term post-ischemic inflammation.

1. Introduction

Ischaemic heart disease, including myocardial infarction (MI), is the main cause of morbidity and mortality for both men and women worldwide [1]. The myocardial injury caused by MI triggers an inflammatory reaction, extending myocardial damage but also a prerequisite to transition toward myocardial healing and scar formation. The extent of the non-contractile scar formed would determine the proclivity to adverse cardiac remodelling, cardiac malfunction and, ultimately, overt heart failure [2]. The current best treatment for heart failure is heart transplantation, but the great demand for organs generated by the growing epidemic of cardiac-related diseases is presently unmet [3,4]. This urges therapies focused on preserving cardiac function after injury, such as cell-based therapies and tissue engineering approaches aimed at modulating post-MI inflammation to mitigate myocardial scarring [5]. For that purpose, the administration of mesenchymal stromal cells (MSC) has been studied to promote healing of ischaemia-injured tissue given their immunomodulatory and regenerative capabilities [6–9]. In this context, our laboratory was the first to pose attention to a population of cardiac adipose tissue-derived MSC (cATMSC) which, despite residing in an adipocytic environment, do not differentiate into adipocytes but acquire *de novo* cardiac and endothelial markers *in vitro* (both human and porcine cells), and contribute to myocardial tissue revascularisation and infarct size reduction *in vivo* [6,7,10,11]. Moreover, their combination with decellularized cardiac tissue as natural three-dimensional (3D) scaffolds is a promising tissue engineering strategy to locally deliver MSC and enhance their therapeutic effect to restore cardiac function after MI [7,10,12,13]. In pre-clinical studies, these engineered cardiac grafts have significantly improved ventricular function, showing scaffold integration with the underlying myocardium, and induced neovascularization and innervation [12,13]. Nevertheless, scarcely any cell grafted into the host myocardium.

At the same time, the current deficits understanding the mechanistic action of cell therapy for cardiac repair and regeneration limits its potential, optimization, and clinical implementation [14]. Numerous evidences suggest that MSC may promote MI healing thanks to the secretion of various soluble factors that boost endogenous repair in a paracrine manner, rather than replicating and differentiating themselves [15,16]. Amongst them, there is growing interest in MSC's release of extracellular vesicles (EV), a variety of lipid bilayered nanovesicles having the biological characteristics of the originating cells, and containing a plethora of functional lipids, RNA, and proteins [17]. EV can transfer these bioactive molecules, and thus are valuable mediators of in intercellular communication. In this context, we corroborated EV as functional players of the paracrine immunosuppressive capability of MSC [18]. However, the mode of action of EV and the optimal administration route to enable sufficient EV dose to be locally active remain unknown.

In the present study, we explored the anti-inflammatory and healing effects of porcine MSC-EV, unravelling a new role of MSC-EV as recruiters of endogenous pro-angiogenic cells, and developed novel potency assays for porcine MSC-EV. Also, we designed a new method for the local delivery of multifunctional MSC-EV over the ischemic myocardium in a pig model of MI, by using a 3D-bioengineered scaffold showing high EV-embedding capacity, local release and modulation of post-ischemic inflammation *in vivo*.

2. Materials and methods

2.1. Porcine cardiac adipose tissue-derived MSC isolation and culture

Primary porcine cATMSC were obtained from pigs (Large White × Landrace) undergoing cardiac surgery ($n = 39$) by cardiac adipose biopsy (1.63 ± 0.69 g), as previously described [7]. Tissue samples were washed from debris and red blood cells in phosphate-buffered saline (PBS; Oxoid), and digested for 30 min with 0.05% collagenase (Type II; Gibco Invitrogen Corp.) at 37 °C under mild shaking. Digestion was quenched with α-MEM (Sigma Aldrich) supplemented with 10% heat-inactivated foetal bovine serum (FBS), 2 mM L-glutamine, 1% penicillin-streptomycin (P/S) (all from Gibco Invitrogen Corp.) and 5 µg/ml Plasmocin™ (Invivogen) (α-MEM-FBS). Cells were then centrifuged at 1200×*g* for 10 min and cultured by adherence in α-MEM-FBS at 37 °C 5% CO_2. The purity of established cell cultures was analysed at passages 4–8 by immunostaining with monoclonal antibodies against CD105 (Abcam), CD44, CD45, CD14 (AbD Serotec), CD29, CD34, CD90 and CD106 or IgG isotype control (BD Pharmingen) using a FACSCanto II flow cytometer (BDBiosciencies) and the FACSDiva™ software (BD Biosciencies).

2.2. Extracellular vesicle production and isolation

EV were produced and isolated as previously published [18,19]. All relevant data regarding our experiments have been submitted to the EV-TRACK knowledgebase (EV-TRACK ID: EV200061) [20].

Serum-derived bovine EV were depleted by ultracentrifuging 2 × α-MEM-FBS at 100,000×*g* for >16 h (TH641 rotor, adjusted k-Factor = 240.82) in a Sorvall WX Ultra 100 Series ultracentrifuge (Thermo Fisher Scientific). The supernatant was filtered through 0.22-µm (Sarstedt) for sterilization, and diluted to a 1 × working solution with α-MEM medium.

For EV production, the culture media of two T-175 flasks of porcine cATMSC grown to confluence was replaced by 15 mL each of EV-depleted α-MEM-FBS. After 48 h of culture, the conditioned medium was harvested and centrifuged at 400×*g* for 5 min and 2000×*g* for 10 min to exclude cells and debris, respectively. Cells were counted at time of EV harvesting (~1×10^7), and cell viability was >95% (trypan blue staining). The cleared supernatant was then centrifuged at 2000×*g* for 35 min through a 100-kDa ultrafiltration device (Amicon Ultra centrifugal filter; Millipore) to obtain concentrated conditioned medium (CCM).

EV were then purified from the CCM by size-exclusion chromatography (SEC) following our already published method [18,21,22]. Briefly, the SEC column was prepared packing 12 mL of Sepharose CL-2B (Sigma Aldrich) into a sterilized Puriflash dry load 12G flash column (Interchim-Cromlab). Then, 500 µL CCM were loaded into the column and eluted with sterile 10% sucrose (w/v; Sigma Aldrich) as an elution buffer, collecting 500-µL fractions immediately after loading. Protein elution was monitored by 280 nm absorbance (Nanodrop spectrophotometer; Thermo Fisher Scientific) or using the Pierce BCA Protein Assay kit (ThermoFisher), interpolating to a Bovine Serum Albumin (BSA; Sigma Aldrich) standard curve. Bead-based flow cytometry was routinely performed to pool together the CD44$^+$CD63$^+$ EV-containing fractions (EV pool) for use in further experiments.

2.3. Bead-based flow cytometry

Porcine cATMSC-EV were identified by bead-based flow cytometry, screening for EV and MSC markers. EV were covalently coupled to 4-µm aldehyde/sulphate-latex beads (Invitrogen-ThermoFisher Scientific) with a 15 min incubation, and then blocked for 2 h with BCB buffer (PBS, 0.1% BSA, and 0.01% sodium azide (NaN_3); Sigma Aldrich). EV-coupled beads were centrifuged at 2000×*g* for 10 min and re-suspended in BCB buffer. Next, beads were incubated for 30 min at RT with the fluorochrome-conjugated antibodies anti-CD73-PE and anti-CD90-PE-Cy7 (1:50; both from BD); or the primary Ab anti-CD9 (Clone VJ1/20; 1:10), anti-CD63 (Clone TEA3/18; 1:10), anti-CD81 (Clone 5A6; 1:10), anti-CD29 (1:10; BD), anti-CD44 (1:10; AbD Serotec) or IgG isotype control (1:10; Abcam) followed by incubation with the FITC-goat F(ab') 2 anti-mouse IgG (1:10; Bionova) or A488-rabbit anti-rat IgG (1:100; AbD Serotec). EV-coupled beads were washed with BCB buffer and spun down at 2000×*g* for 10 min after each step. Data was acquired in a FACSVerse flow cytometer (BD), and analysed with FlowJo® v10 (BD).

2.4. Cryo-electron microscopy

EV size and morphology were examined by cryo-transmission electron microscopy (cryo-EM) as previously detailed [18].

2.5. Nanoparticle tracking analysis

Size distribution and particle concentration was analysed in a NanoSight LM10-12 instrument (Malvern Instruments Ltd), with NTA software (version 3.1, build 3.1.46) averaging three videos of 60 s at 30 FPS, with a camera level of 16, and manual control of temperature (21-25 °C) of samples diluted to 20–120 particles/frame, as previously reported [18].

2.6. EV staining

Fluorescently-labelled EV were produced by staining EV-secreting cATMSC with the lipophilic dyes NIR815 (excitation/emission 786/815 nm; Thermo Fisher Scientific) or PKH26 (excitation/emission 551/567 nm; Sigma Aldrich) following manufacturers' instructions. Fluorescently labelled cells were washed with PBS, cultured in α-MEM-FBS and then changed to EV-depleted medium to produce fluorescently-labelled EV, which were isolated from the conditioned medium using the already described methodology.

2.7. Endotoxin detection

The endotoxin concentration of cATMSC-EV preparations was determined using the Pierce Chromogenic Endotoxin Quant Kit (ThermoFisher) following the manufacturer's instructions. Briefly, the endotoxin concentration was determined for EV at 1×10^6 cATMSC/ml in a Limulus Amebocyte Lysate (LAL)-based chromogenic reaction using an *E. coli* (011:B4) endotoxin standard curve and analysing different sample dilutions. The absence of LAL inhibition was confirmed in endotoxin spike-in reaction.

2.8. Porcine peripheral blood mononuclear cells isolation and functional assays

Peripheral blood mononuclear cells (PBMC) were obtained by Ficoll density gradient centrifugation (BD) of fresh whole blood samples (10-mL EDTA tubes; BD) from Landrace × Large White pigs (30–35 kg; indistinct sex). After harvesting, PBMC were counted and frozen. To monitor proliferation, thawed PBMC were labelled with Violet CellTrace™ dye (Thermo Fisher Scientific) following manufacturer's protocol. Then, PBMC were seeded in 96-well plates at 1×10^5/well; 100 μl final volume of serum-free X–VIVO 15 media (Lonza) complemented with 2 mM L-glutamine and 1% P/S.

PBMCs were stimulated with 0.6 ng/mL PMA (phorbol 12-myristate 13-acetate; Sigma Aldrich) and 200 ng/mL ionomycin (Io; Sigma Aldrich), in the presence or not of cATMSC-EV (pool of three cATMSC donors), at the indicated ratios according to EV-producing cell equivalents (1×10^6/well, 2×10^5/well, 1×10^5/well or 4×10^5/well). After 5 days of culture, supernatants were collected and frozen for downstream cytokine production analysis, and the number of FSC^{high}Violet^{low} proliferating cells was assessed by flow cytometry with an LSRFortessa (BD) and FlowJo® v10 software.

Alternatively, 1×10^5 PBMC were cultured together with cardiac scaffolds (7.1 mm^2) filled with peptide hydrogel and either cATMSC-EV (1×10^6 EV-producing cells/scaffold) or 10% sucrose buffer. After 5 days of culture, supernatants were harvested for cytokine production analysis.

2.9. Cytokine response

The levels of IL1β, IL4, IL6, IL8, IL10, IL12p40, IFNα, IFNγ, and TNFα were measured in the supernatants of cultured PBMC using the Cytokine & Chemokine 9-Plex Porcine ProcartaPlex™ Panel 1 immunoassay (Invitrogen-ThermoFisher Scientific) in a Luminex 200 Instrument, and analysed with the xPONENT software (build 3.1.971.0) following manufacturers' instructions.

2.10. Porcine outgrowing endothelial progenitor cell cultures and characterization

Outgrowing colonies from endothelial progenitor cell cultures were isolated by processing fresh 20-mL venous blood samples (<2 h) from pigs (Landrace × Large White; 30–35 kg; indistinct sex) by Ficoll gradient (GE Healthcare) as previously described [23]. Remaining erythrocytes were removed with lysis buffer (155 mM NH$_4$Cl, 10 mM NaHCO$_3$, and 0.115 mM EDTA), PBMC were re-suspended in endothelial growth medium-2 (EGM-2; Clonetics®), seeded at 2×10^7 cells/mL in fibronectin-coated plates (10 μg/mL; Sigma-Aldrich), and cultured with media replacement every 2–3 days. Late outgrowth endothelial cell (OEC) colonies with clonogenic capacity were visible after 14 days in culture, further expanded and frozen in liquid nitrogen until further use.

OEC immunophenotyping was performed by fixing cells with 4% paraformaldehyde (Sigma Aldrich) for 15 min, washing with 0.1% Tween-PBS (T-PBS), blocking for 1 h (1% BSA in T-PBS), and then incubating at 4 °C for 16 h with the primary antibodies anti-VEGFR2 (1:50; Santa Cruz Biotechnology), anti-CD31 (1:50; Abcam), and anti-vWF (1:100; Sigma Aldrich). After washing with T-PBS, cells were incubated with the secondary antibodies AlexaFluor® 488 and AlexaFluor® 568 (1:1000; Invitrogen) for 1 h at RT and counterstained with Vectashield® mounting medium with DAPI (Vector Laboratories, Inc.) prior to visualization in an Olympus BX61 microscope (Olympus).

Alternatively, OEC were blocked with 25% AB human serum (Sigma-Aldrich) in 1% BSA and 0.1% NaN$_3$ in PBS for 15 min at RT, and labelled with anti-CD34-PE (BD) for 30 min at RT. After washing and filtering through a 30-μm filter (Partec), cells were analysed in a FACSAria flow cytometer (BD) to confirm their hematopoietic/progenitor origin.

The capacity of OEC to form vessel-like structures was evaluated in an *in vitro* Matrigel assay. 200 μL of ice-cold Matrigel™ (growth factor-reduced; BD) was placed in 24-well plates and incubated at 37 °C for 30 min. Then, 4×10^4 OEC were seeded in EGM-2. After 24 h, images were taken using the Olympus IX71 microscope (Olympus).

2.11. Migration assay

Cell migration driven by EV was measured in agarose spots using an adaptation of a previously published protocol [24,25]. Beforehand, wells dedicated to OEC were coated with 10 μg/mL fibronectin (Biochrom) and left dry. In each quadrant drawn in wells of 6-well plates, we placed three 5-μL droplets of 0.5% low-melting-point agarose (40 °C, Ecogen) mixed 1:1 (v/v) with either 10% sucrose, vascular endothelial growth factor (VEGF; 50 ng/mL final concentration; Sigma Aldrich), or cATMEC-EV (8×10^4 or 4×10^4/spot). The plates were placed at 4 °C for 15 min to promote gel solidification and spot adherence to the plate surface. Next, either cATMSC in α-MEM-FBS or OEC in EGM-2 complete medium (10% FBS), were poured into the corresponding wells and allowed to seed for 3 h at 37 °C. To limit cell proliferation and favour chemoattractant detection by cells, culture media was replaced with low serum supplemented medium (0.2% FBS).

Localizations of the border of the agarose spots were randomly picked to take pictures (3 × 3 mosaic at 20 × objective) every hour for 21 h with an Axioskop Z1 microscope (Zeiss), under controlled temperature and CO$_2$ level. We compiled the images to videos, and random cells were followed using the *Manual tracking* plug-in Fiji software (Image J 1.54w, NIH) and the Chemotaxis and Migration tool software version 2.0 (Ibidi, Inc.) to quantify distance, velocity, and directionality of cell movement.

2.12. Tube formation assay

OEC tube formation capacity was measured in 24-well plates precoated with 200 μL/well of ice-cold Matrigel (Corning). OEC (2×10^4 cells/well) were seeded in complete EGM-2 media without VEGF (Lonza) in the presence of cATMSC-EV (2×10^6/ml, 1×10^6/ml or 4×10^5/ml EV-producing cells), or VEGF (200 ng/mL; R&D systems) as a positive control. Cells were incubated for 6 h at 37 °C 5% CO_2 and images were taken with a phase contrast inverted microscope at 10 × objective magnifications and analysed using the Fiji (ImageJ) Angiogenesis Analyser plugin.

2.13. Generation of cardiac scaffolds

Cardiac scaffolds were generated by decellularisation of either human pericardial or porcine myocardial tissues. The formers were 19 healthy pericardial samples from patients ($n = 19$; 16 males, 3 females; mean age, 65 ± 12 years; range, 44–85 years) who were undergoing cardiac interventions at our hospital, and who had given their signed consent. The local ethics committee revised and approved this study, whose protocols conformed to the principles outlined in the Declaration of Helsinki. Additionally, we used a total of 21 myocardial scaffolds obtained from porcine heart left ventricles from a slaughterhouse (Landrace × Large White pigs; $n = 4$).

We proceeded with a detergent-based decellularisation (SDS and Triton X-100) of either cardiac tissue, followed by DNase I treatment, lyophilisation, and sterilization as previously detailed by our group [7, 26]. Scaffold size was standardised to 7.1 mm² and 50.3 mm² using disposable 3-mm and 8-mm biopsy punches respectively, or to 2 cm² by using a scalpel.

2.14. EV delivery into decellularised scaffolds

The EV pool, corresponding to a specified number of producing cATMSC, was concentrated with a sterile 2-mL 100-kDa ultrafiltration device (Merck Millipore) to adjust its final volume according to the size of the intended scaffold, using 10% sucrose buffer (see Fig. S5). Adjusted EV volume was then mixed (1:1, v/v) with 0.3% PuraMatrix® self-assembling peptide hydrogel (Corning) in 10% sucrose, and this mixture was laid over the lyophilised, decellularised scaffolds to both rehydrate and fill the scaffolds with EV. As control, 10% sucrose buffer was mixed (1:1, v/v) with the peptide hydrogel. Specifically, a 4.2 μl mix (containing hydrogel and cATMSC-EV from 1×10^6 EV-producing cells) was added to 3-mm ⌀ scaffolds and used to analyse its influence on allogeneic PBMC cytokine response; a 100 μl mix (containing hydrogel and cATMSC-EV from either 1×10^5 or 1×10^6 EV-producing cells, previously stained with either NIR815 or PKH26) was added to 8-mm ⌀ scaffolds to assess EV retention by NIR815-EV scanning, PKH26-EV confocal microscopy analysis or by scanning electron microscopy (SEM); and a 200 μl mix (containing hydrogel and EV from 20×10^6 EV-producing cATMSC previously stained with NIR815) was added to 2 cm² scaffolds for *in vivo* implantation over the ischemic area of the MI porcine model. After 15 min of seeding and scaffold rehydration at RT, culture medium was added over scaffolds to promote the salt-triggered peptide folding and consequent self-assembling hydrogel jellification for a minimum of 30 min and up to 2 h at 37 °C before use.

2.15. Near-infrared scaffold scanning

To check cATMSC-EV retention in scaffolds and tracking *in vivo*, EV were produced from NIR815-labelled cATMSC. EV-associated labelling was confirmed by performing a dotblot assay of each SEC elution fraction and of the concentrated EV pool, placing 5 μl/spot by superimposing 1 μl-drops, and scanning for NIR815 fluorescence in an Odyssey CLx (LI-COR Biosciences, Inc.). Then, cATMSC-EV retention was monitored by scanning NIR815-labelled EV-loaded 8-mm ⌀ cardiac scaffolds in an Odyssey

CLx, detecting the near-infrared fluorescent dye NIR815 and autofluorescence in the 800-nm and 700-nm channels, respectively. To confirm cATMSC-EV scaffold loading right before implantation, pericardial scaffolds were scanned in a Pearl Impulse Imager (Li-COR).

2.16. Scanning electron microscopy

To confirm cATMSC-EV presence within scaffolds, cardiac scaffolds loaded with NIR815-labelled EV were maintained for 1 week at 37 °C, 5% CO_2, after which they were washed with PBS and processed for SEM. Briefly, after fixation with 10% formalin (Sigma Aldrich) and washing with distilled water, scaffolds were dehydrated in ethanol solutions of increasing concentrations, and dried using a CO_2 critical point dryer (EmiTech K850; Quorum Technologies), as detailed previously [26]. The scaffolds were then sputter-coated in gold using the JFC 1100 ion sputter (Jeol), and scanned under a JSM-6510 scanning electron microscope (Jeol) at 15 kV.

2.17. Myocardial infarction pig model

Animal studies were approved by the local Animal Experimentation Ethical Committee and Government Authorities (Generalitat de Catalunya; Code:10547), and comply with the guidelines defined by the Guide for the Care and Use of Laboratory Animals [27]. Eight crossbreed Landrace x Large White pigs (31.3 ± 1.5 kg) were subjected to MI and randomly distributed into control (n = 4; implantation of hydrogel-alone filled scaffold) or treated group (n = 4; implantation of cATMSC-EV with hydrogel-filled scaffold).

Animals were sedated with an intramuscular (IM) injection of atropine (0.04 mg/kg; BBraun) and pre-anesthetized with dexmedetomidine (0.03 mg/kg, IM; Dexdor®, Orion Pharma), midazolam (0.3 mg/kg, IM; Laboratorios Normon), and butorphanol (0.3 mg/kg, IM; Butomidor®, Richter Pharma AG). Then, anaesthetic induction was performed with an intravenous (IV) bolus of propofol (2 mg/kg; Propovet®, Zoetis). Animals were endotracheally intubated, and anaesthesia was maintained by 2% isoflurane (IsoVet®, BBraun) inhalation. Fentanyl (0.075 mg/kg/45 min, IV; Fentadon®, Dechra) and an IV 1.5 mg/kg atracurium besylate bolus (Sanofi Aventis S.A.) were administered during intervention. After a left lateral thoracotomy, a double-ligation of the first marginal branch of the circumflex artery, 1.5 cm distally from the atrioventricular groove (Optilene 5/0 W-8556 12-S, Ethicon Inc.) was performed to induce MI. After 30 min, a pericardial scaffold, with or without NIR815-labelled cATMSC-EV (from 20×10^6 EV-producing cells), was placed over the infarcted myocardium and secured with 0.1–0.2 mL of surgical glue (Glubran2®, Cardiolink S.L.). Tulatromicin (2.5 mg/kg, IM; Draxxin®, Pfizer Animal Health) was administered at the end of the surgery as antibiotherapy and a transdermal fentanyl patch was applied as an analgesic post-operative care (Durogesic®, Janssen-Cilag). Finally, pigs were recovered, and housed until experimental end-point.

2.18. Tissue collection, morphometric and histopathological analyses

Six days after MI induction, animals were euthanized by administering sodium thiopental overdose (200 mg/kg) and porcine hearts were excised, then scanned in a Pearl Impulse Imager (Li-COR), sectioned and scanned again for EV tracing within heart sections (Fig. S7). Heart samples, including infarct core, border zones and healthy myocardium were either fixed in 10% formalin for paraffin inclusion or embedded in OCT (VWR) and snap-frozen in liquid nitrogen-cooled isopentane.

Descriptive histopathological analysis and scar fibrosis were analysed in 5-μm paraffin sections with Masson's trichrome and Picrosirius red staining, respectively, as described previously [28]. Total collagen, and specifically collagen type I and III were quantified in six random fields of each tissue section using Image-Pro Plus software (6.2.1 version; Media Cybernetics, Inc.).

2.19. Immunohistochemical analysis

To examine cATMSC-EV retention within scaffolds by confocal microscopy, immunostaining was performed in PKH26-EV loaded scaffolds. Specifically, cardiac scaffolds with PKH26-labelled EV incubated for 2 h were thoroughly washed 3 times with PBS, fixed with 10% formalin for 1 h at RT, rinsed 3 times with PBS, embedded in OCT and snap-frozen in liquid nitrogen-cooled isopentane. Also, decellularisation was confirmed by performing immunostaining on 10-μm-thick native and decellularised tissue cryosections. Succinctly, after blocking for 1 h at RT with TBS (Tris-buffered saline)/0.2% Triton-X-100/10% horse serum/1% BSA (all from Sigma Aldrich), tissue sections were incubated overnight at 4 °C with phalloidin-Atto 565 (Phal565; 1:500; Sigma) and primary antibody against cardiac troponin I (cTnI; 1:100; Abcam) and type-III collagen (col-III; 1:100; Abcam). Sections were then incubated for 1 h at RT with Cy2-, Cy3-, and Cy5-conjugated secondary antibodies (1:500; Jackson ImmunoResearch Laboratories), respectively, and nuclei counterstained with DAPI (0.1 μg/mL; Sigma-Aldrich).

Vascular density in the MI pig model was analysed in 10-μm OCT-embedded tissue cryosections immunostained with biotinylated *Griffonia simplicifolia* Lectin I isolectinB4 (IsoB4; 1:50; Vector Labs) and Streptavidin-Alexa488 (1:500; Invitrogen). Macrophage, B and T cell infiltration was also analysed by immunostaining tissue cryosections using cTnI (Abcam) and CD163 (Novus Biologicals) or CD20 (Biocare medical), CD3 and CD25 (both from AbD Serotec) primary antibodies (1:100), followed by incubation with the Alexa Fluor 488-, Alexa Fluor 647- (Molecular Probes) and Cy3- (Jackson ImmunoResearch Laboratories) conjugated secondary antibodies (1:500) and nuclei counterstaining with DAPI.

Immunofluorescence images were acquired in an Axio-Observer Z1 confocal microscope (Zeiss). Quantitative measurements of blood vessel area (IsoB4 staining) in either the infarct core or scaffold were performed using Image-Pro Plus software in six different random fields per section. Quantification of CD163$^+$, CD20$^+$, CD3$^+$ and CD25$^+$ cells, was carried out by two independent investigators measuring at least four different optical fields from each section.

2.20. Statistical analysis

Data is shown as mean with SD unless stated otherwise. Statistical differences are shown when found significant ($p < 0.05$) applying the appropriate statistical tests for each dataset after checking for normality of data, using Graphpad Prism (6.0 version) and SPSS 21.0.0.0 (SPSS, Inc, Chicago, IL) softwares.

3. Results

3.1. Porcine cATMSC-EV purification

Primary cultures of porcine cATMSC were established and validated as positive for CD29 (84%), CD44 (88%), CD90 (99%) and CD105 (92%) and negative for CD14, CD34, CD45 and CD106 [7]. EV were then isolated from cell- and debris-cleared conditioned media of porcine cATMSC cultures by SEC. cATMSC-EV were screened for EV markers (CD9$^+$ CD63$^+$ CD81^{low} CD5L^{low}) and MSC markers (CD44$^+$ CD29^{low} CD73^{low} CD90^{low}) (Fig. S1), being CD63 and CD44 the most relevantly and consistently detected. Thus, they were routinely used to track porcine cATMSC-EV elution in the SEC fractions (Fig. 1A). Isolation by SEC ensured EV purification from the rest of soluble factors present in cATMSC conditioned media, as previously published [18]. We pooled the CD63$^+$CD44$^+$ fractions, containing porcine cATMSC-EV, and confirmed by cryo-EM the double membrane, round shape, and nanovesicle size of cATMSC-EV (Fig. 1B and C). Furthermore, EV mean diameter by NTA was 211.2 (14.66) nm (Fig. 1D and E), and the concentration of particles according to NTA was homogeneous after normalisation by the EV-producing cell numbers at EV harvest (Fig. 1E). Protein concentration in EV pools was really low (0.554 (0.391) μg total protein; 6.94×10^{-02} (7.13×10^{-02}) μg/10^6 cells at EV harvest), and did not correlate well with the EV-producing cell numbers (Fig. S2), thus it was not used to normalise EV numbers. Instead, we used the EV-producing cell numbers at harvest as a proxy of EV quantitation, as we and others previously reported [18,29,30].
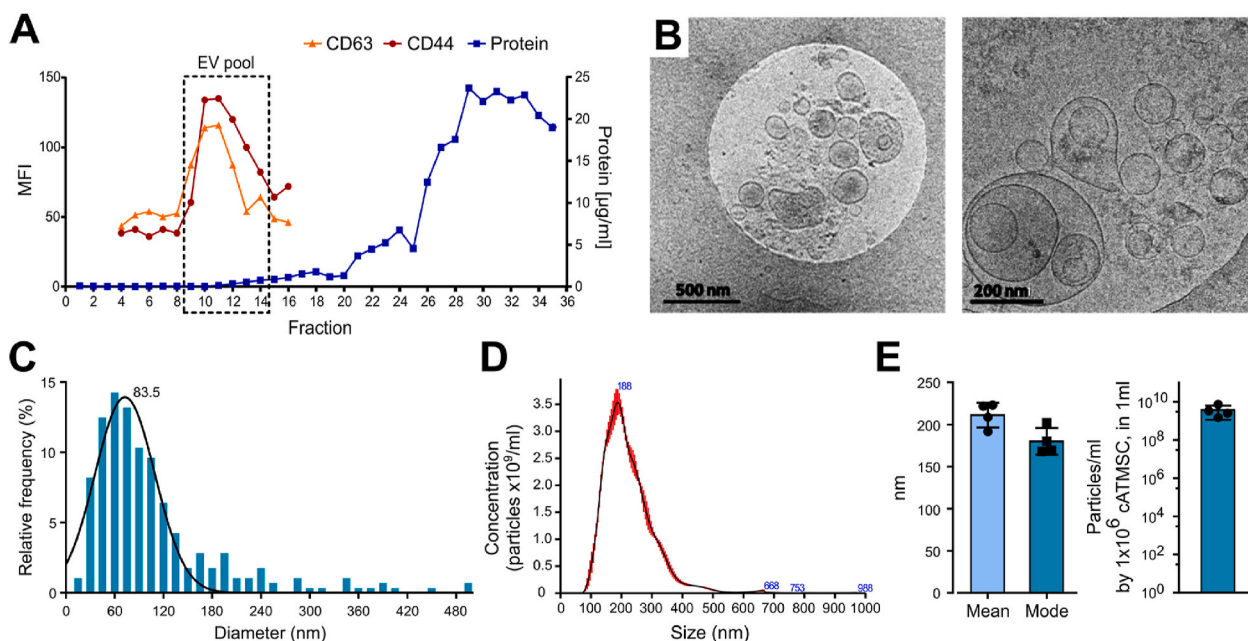
Fig. 1. EV were isolated from porcine cATMSC by SEC, and phenotypical and morphologically characterised. **(A)** Representative SEC elution profile of porcine cATMSC-EV, found in the fractions positive for the EV and MSC markers CD63 and CD44 (MFI, median fluorescence intensity by bead-based flow cytometry). The protein eluted later, measured by BCA. **(B)** Cryo-EM confirmed that porcine cATMSC-EV were double membrane round nanovesicles of 50–300 nm. Scale bars are 500 nm and 200 nm, respectively. **(C)** Histogram depicting the size distribution of cATMSC-EV according to cryo-EM (n = 280). **(D)** Representative histogram depicting size and concentration of EV according to NTA analysis. **(E)** EV diameter by NTA was around 200 nm. Concentration of particles according to NTA, normalised by the EV-producing cell number.

3.2. cATMSC-EV have immune suppressive properties

To test the immunomodulatory properties of cATMSC-EV, we analysed their potency in terms of proliferation and cytokine secretion of allogeneic porcine PBMC modulation by the presence or absence of cATMSC-EV. PBMC were activated with PMA plus Io, that simulated the pro-inflammatory environment found in the ischemic injury post-MI, which led to high PBMC proliferation and an inflammatory cytokine response (Fig. 2). When cATMSC-EV were added to the mix, they dose-dependently suppressed the proliferation of allogeneic PBMC (Fig. 2A). Notably, the capacity of cATMSC-EV to inhibit PBMC proliferation was not dependent on the specific EV pool, but rather on the responder PBMC donor. cATMSC-EV also abrogated the secretion of the pro-inflammatory cytokines IFNγ, TNFα, and IL12p40 in stimulated PBMC (Fig. 2B). IL10 was also reduced by cATMSC-EV. However, the lowest EV dose maintained IL10 production while reducing the pro-inflammatory cytokine levels, thus increasing the IL10:IFNγ ratio. IL6 and IL8 secretion was not modified by cATMSC-EV. Other cytokines, including IL1β, IL4, and IFNα, were found at negligible levels (<10 ng/ml) and did not change by cATMSC-EV presence (data not shown). Notably, the lack of cytokine response to cATMSC-EV from allogeneic PBMC suggested an absence of alloreactivity. The absence of TNFα induction, and actually reduction by cATMSC-EV, suggested that the EV products had low endotoxin levels, as corroborated by endotoxin testing (<2 EU/ml). Nevertheless, this is an important issue to inspect before clinical translation. EV production under GMP conditions and manufacturing in clean room facilities would further reduce the endotoxin levels to fulfil regulatory requirements.

3.3. Porcine cATMSC-EV recruit allogeneic pro-regenerative cells and promote angiogenesis

The success of the local delivery of EV for myocardial repair relies on the hypothesis that EV will recruit endogenous cells towards the infarcted tissue, and among other beneficial effects, promote revascularisation of the injured myocardium. To start validating this hypothesis *in vitro*, we quantitatively analysed the chemotactic action of cATMSC-EV towards allogeneic OEC and MSC in agarose spots, using an adaptation of a previously described protocol [24,25], and their effect on the tube formation capacity of OEC.

Swine OEC were isolated from porcine peripheral whole blood samples. We confirmed them as genuine hematopoietic vascular precursors with specific endothelial-lineage marker expression, such as VEGFR2, vWF, CD31 (immunocytofluorescence; Figs. S3A–C), and CD34 (flow cytometry; Fig. S3D), and formed vascular-like networks when seeded in Matrigel (Fig. S3E).

Then, we analysed the active migration of MSC and OEC towards agarose spots containing increasing doses of cATMSC-EV. While no cells entered the spots containing buffer alone, MSC and OEC invaded the spots containing cATMSC-EV in a dose-dependent manner (Fig. 3 and Supplementary Videos 1–6). Of note, OEC also migrated inside the spots containing VEGF, used as a positive control. OEC and MSC tracking over
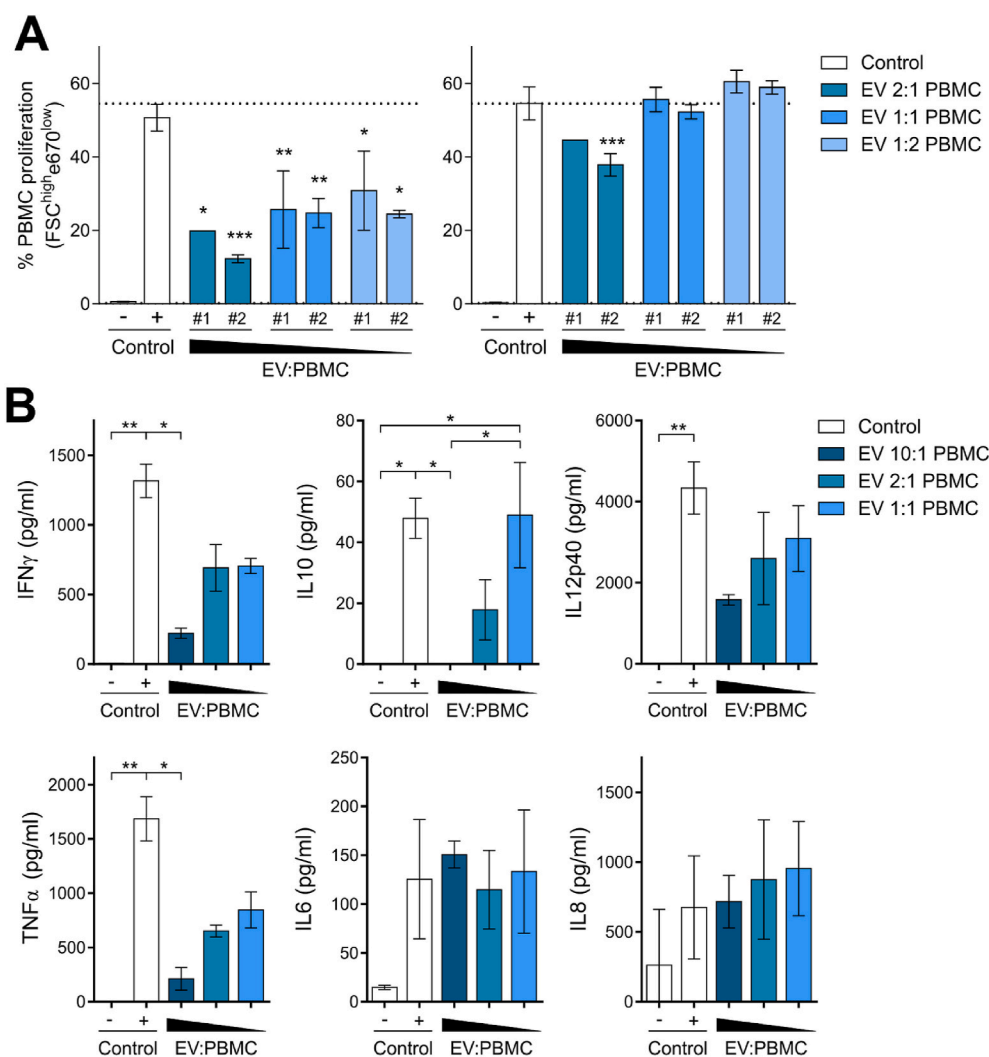
Fig. 2. Porcine cATMSC-EV abrogate polyclonal proliferation and modulate the cytokine response of allogeneic PBMC. **(A)** Two representative EV pools (#1 and #2) were tested in potency assays (doses of 2×10^5, 1×10^5 and 5×10^4 EV-producing cells) against two different fully allogeneic PBMC responders (1×10^5 cells) with polyclonal stimulation (PMA + Io; Control +). Proliferating PBMC were determined according to dye dilution as the percentage of FSC^{high}-$e670^{low}$ cells. Data are shown as mean ± SD. Statistical differences to the positive control (PMA + Io) are indicated as *$p < 0.05$; **$p < 0.01$; ***$p < 0.001$ by Two-way ANOVA with Tukey's multiple comparison test. **(B)** We assessed the cytokine levels in supernatants of the two different fully allogeneic PBMC in the presence or absence of two different cATMSC-EV pools (10:1, 2:1, and 1:1 cATMSC-EV:PBMC ratios) at five days after PMA + Io stimulation. Bars indicate mean ± SD. *$p < 0.05$; **$p < 0.01$ by one-way ANOVA with Dunn's multiple comparison test.

24 h indicated a positive directionality in the cell movement towards the EV-containing spots, demonstrated by an increased Directness of movement and Euclidean distance (Δxy) of cells, while no changes in the Accumulated distance (ΣΔxy) or Velocity of cells was found (data not shown). Also, this was only observed in OEC and MSC in contact with the agarose spot (border *versus* remotely positioned cells; Fig. 3).

Supplementary video related to this article can be found at https://doi.org/10.1016/j.bioactmat.2021.02.026

Secondly, cATMSC-EV were able to promote angiogenesis on allogeneic porcine OEC in a dose-dependent manner (Fig. 4). The number of nodes and branch length increased with EV dose, and thickened vascular-like meshes were observed in the highest EV doses analysed. Of note, the EV concentration range was equal to that used in the proliferation assays.

3.4. Biocompatible 3D-Engineered scaffolds maintain the internal ultrastructure and are devoid of cells after decellularisation

Two decellularised cardiac scaffolds were generated from either human pericardial or porcine myocardial tissues, with their intrinsic structure preserved, including the spatial 3D organization of the native matrix fibrils (Figs. S4A–D). Complete decellularisation was confirmed in both pericardium and myocardium by the absence of actin (Figs. S4E–F) and cardiac troponin I (Figs. S4G–H), respectively, and removal of cell nuclei in both acellular scaffolds (Figs. S4F and H). Additionally, the positive staining for type-III collagen (Figs. S4E–H), proved the preservation of extracellular matrix (ECM) protein components following decellularisation, as previously described [12]. Moreover, as we previously published, a proteomic characterization of decellularised pericardial and myocardial scaffolds revealed the presence of matrisome/ECM-related proteins, including major cardiac ECM components like ECM glycoproteins and regulators, collagens and proteoglycans, consistent to their corresponding native tissues [12].
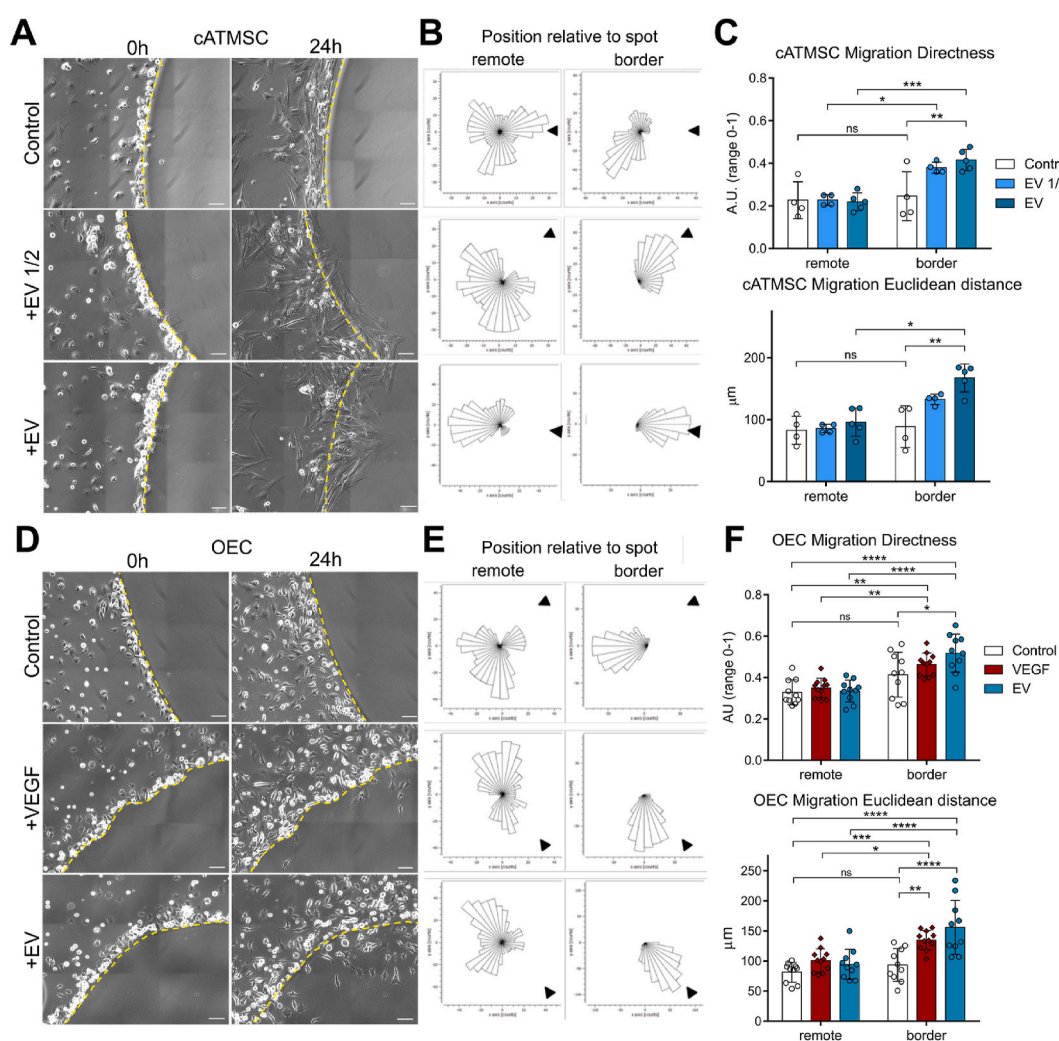
Fig. 3. Porcine cATMSC-EV recruit allogeneic swine cATMSC and swine peripheral blood OEC. **(A–C)** Allogeneic cATMSC were added to plates with agarose spots containing increasing doses of cATMSC-EV (from 4×10^4 and 8×10^4 cells), and cell migration was assessed over 24 h. **(D–F)** OEC were added to plates with agarose spots containing VEGF (positive control) or cATMSC-EV (from 8×10^4 cells), and cell migration was assessed over 24 h. **(A, D)** Representative images of agarose spot borders (dotted line) at 0 and 24 h. Migrating cells are observed only inside spots containing EV or VEGF. Scale bars = 100 μm. **(B, E)** The corresponding rose plots of cell movement during the 24-h time-lapse. Arrow cap indicates direction to the spot. The border and remote positions were determined at 0 h for cells localised or not in the border of the agarose spot, respectively. **(C, F)** Directness and Euclidean distance (Δxy) of cell movement. Pictures were taken hourly, tracking ten cells in each position of at least three spot positions tracked for each condition. **(A–C)** N = 2 independent experiments. *$p < 0.05$, **$p < 0.01$, and ***$p < 0.001$ by two-way ANOVA with Tukey's post-hoc analysis. **(D–F)** N = 3 independent experiments. *$p < 0.05$, **$p < 0.01$, ***$p < 0.001$, and ****$p < 0.0001$ by two-way ANOVA with Tukey's post-hoc analysis.
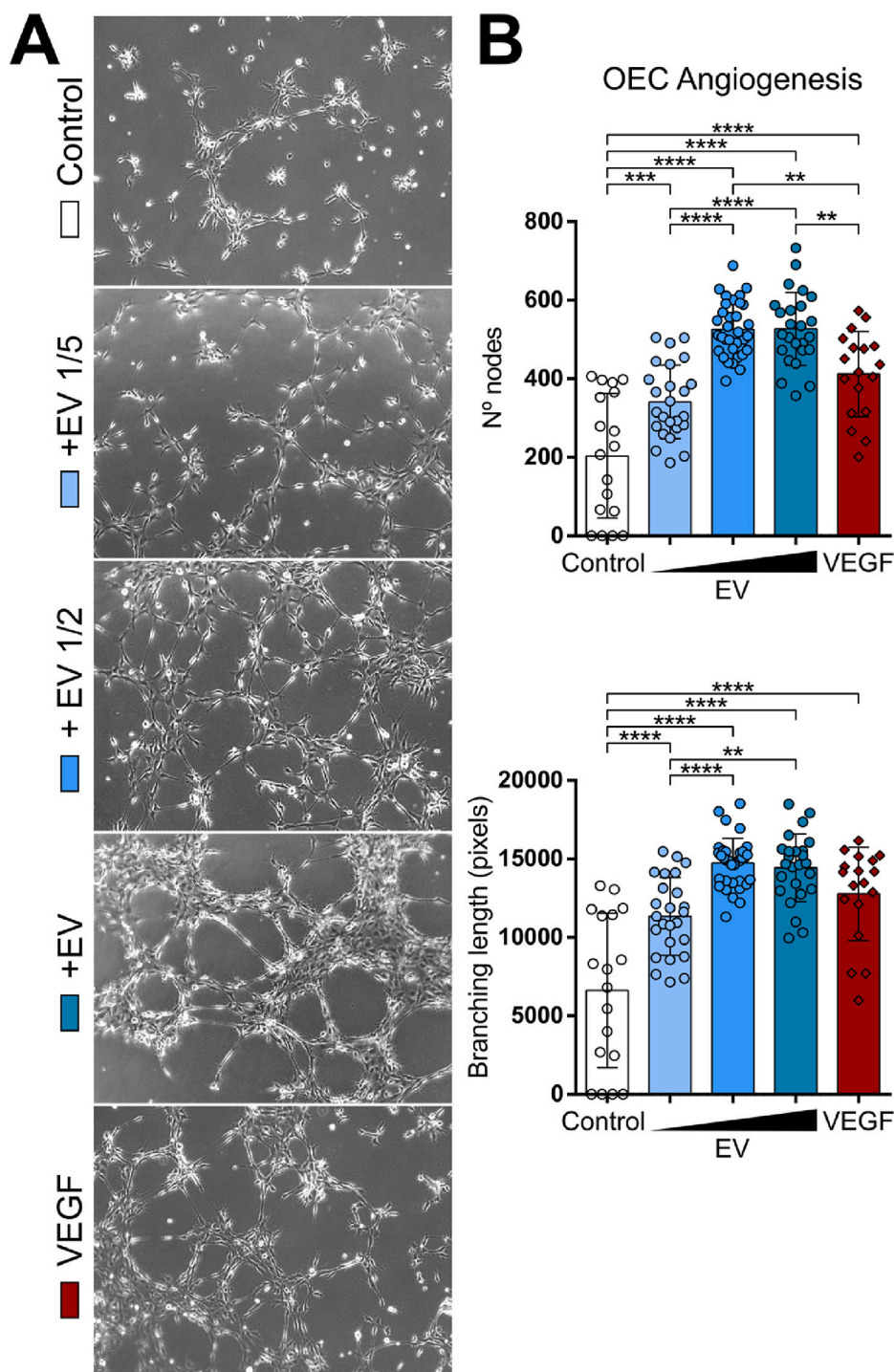
Fig. 4. Porcine cATMSC-EV promote angiogenesis to allogeneic swine peripheral blood OEC. OEC were seeded in Matrigel-coated wells, with increasing doses of cATMSC-EV (2×10^6/ml, 1×10^6/ml or 4×10^5/ml producing cells) or VEGF (200 ng/mL). **(A)** Representative images at 6 h, showing an increased number of junctions and thickening of the vascular-like networks with increasing EV doses. **(B)** Tube formation was quantified in terms of Number of nodes (top) and Branching length (bottom). Data includes 2 independent experiments, each with 3 biological replicates and 2 technical replicates each. $**p < 0.01$, and $***p < 0.001$ and $****p < 0.0001$ by One-way ANOVA with Tukey's post-hoc analysis.

3.5. Porcine cATMSC-EV are successfully retained within 3D-Engineered cardiac scaffolds

To assess the feasibility of EV delivery through confinement in 3D-engineered cardiac scaffolds, we first evaluated EV retention within the scaffolds. For that, we loaded the decellularised, lyophilised scaffolds with cATMSC-EV mixed with self-assembling peptide hydrogel, necessary to enhance scaffold rehydration and ensure filling with EV (Fig. S5). EV were fluorescently stained for tracking with lipophilic dyes, but to avoid troublesome EV washing and carry-over of lipophilic dye aggregates from labelled EV, the EV-producing cATMSC were labelled instead, enabling the tracking of fluorescently-labelled EV. NIR815 EV-associated labelling was confirmed by performing a dotblot of each SEC elution fraction, scanning fluorescence at 800 nm (Fig. 5A). The NIR815 fluorescent signal was increased after concentrating the EV pool by 100 kDa ultrafiltration (Fig. 5A, right). Then, the concentrated EV pool was mixed with self-assembling peptide hydrogel, and used to fill and rehydrate lyophilised pericardial and myocardial scaffolds. After the salt-triggered hydrogel jellification, scaffolds were thoroughly washed with PBS and near-infrared fluorometric scanning revealed cATMSC-EV retention in both 3D-bioengineered cardiac scaffolds (Fig. 5B). Noteworthy, pericardial scaffolds held higher amounts of EV according to fluorescence intensity quantification and visible in the scanned images, observing an earlier saturation of myocardial scaffolds (Fig. 5C). Of
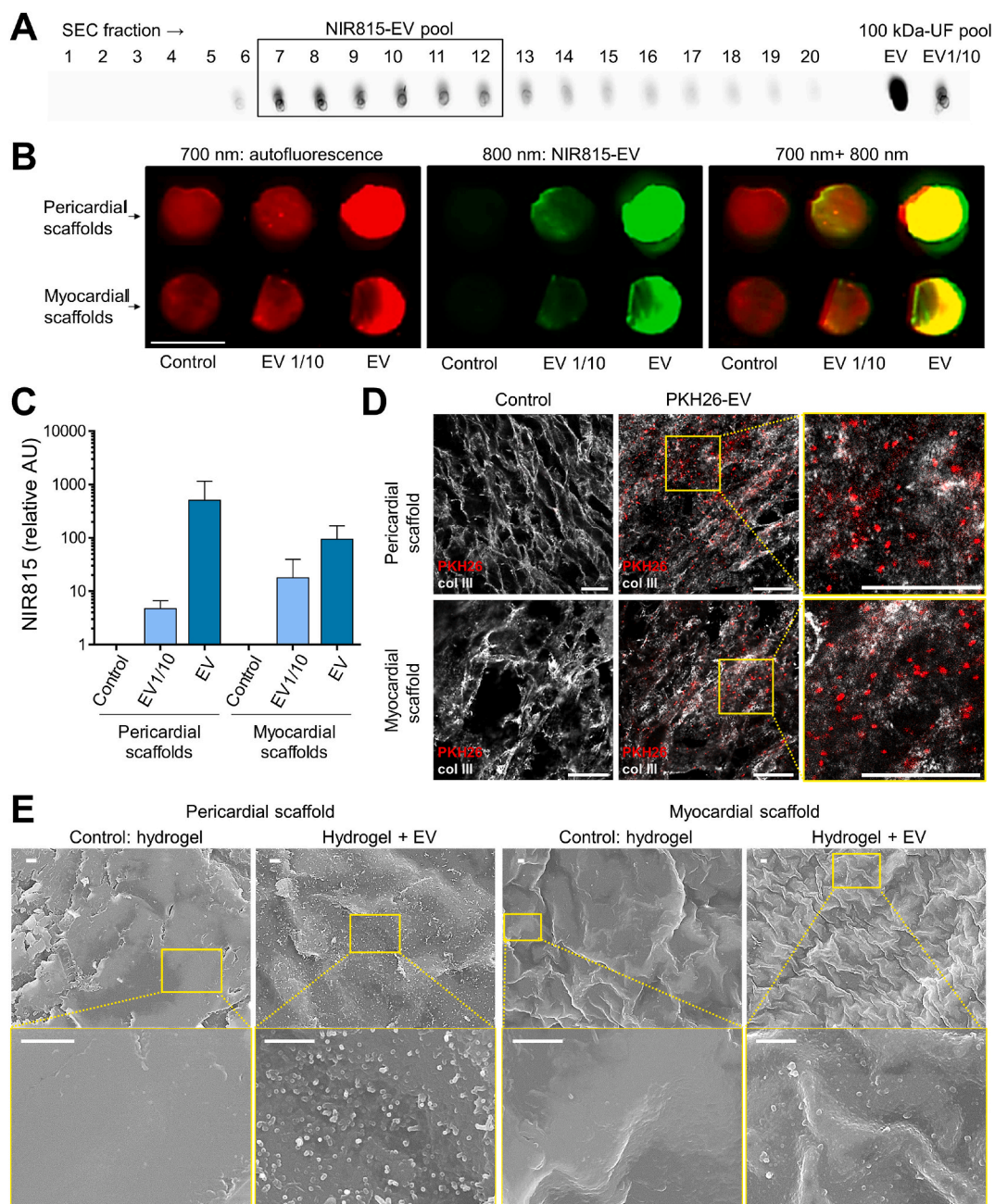
Fig. 5. Engineered cardiac scaffolds retained cATMSC-EV, as shown by fluorometric scanning, confocal microscopy and SEM imaging. **(A)** Dotblot of SEC fractions eluting NIR815-labelled porcine cATMSC-EV, scanning fluorescence at 800 nm. EV-containing fractions (squared) were confirmed NIR815+, pooled together and concentrated by 100 kDa-ultrafiltration, maintaining NIR815 fluorescence (right). **(B–C)** NIR815-labelled cATMSC-EV mixed with peptide hydrogel and added to pericardial and myocardial scaffolds were detected after thorough washing of scaffolds. **(B)** Representative near-infrared fluorescent scanning images of pericardial and myocardial scaffolds (autofluorescence at 700 nm, red) embedded with NIR815-cATMSC-EV (NIR815 fluorescence at 800 nm, green). Scale bar = 1 cm. **(C)** NIR815-cATMSC-EV fluorescence quantification expressed as relative to hydrogel-alone filled scaffold (background). **(D)** PKH26-labelled cATMSC-EV (red) were detected inside the scaffolds by confocal imaging, after immunostaining for collagen III (col III; grey). Scale bar = 20 μm. **(E)** SEM imaging confirms retention of porcine cATMSC-EV within scaffolds after washing and week-long culture, appearing as 100–120 nm protuberances embedded in the hydrogel filling the scaffolds. Controls are scaffolds filled with peptide hydrogel alone. Scale bar = 1 μm.

note, both scaffolds released the EV with time (Fig. S6).

To corroborate cATMSC-EV retention inside the scaffolds, we loaded them with PKH26-labelled cATMSC-EV, following the same aforementioned procedure. Indeed, confocal microscope imaging of scaffold midsections revealed cATMSC-EV presence within the scaffolds (Fig. 5D). Moreover, even after thorough washing and a week-long culture at 37 °C, cATMSC-EV were found inside the scaffolds as confirmed by SEM, distinguishable as 100- to 120-nm protuberances embedded in the hydrogel filling the scaffolds (Fig. 5E).

3.6. Porcine cATMSC-EV combined with cardiac scaffolds abrogate the cytokine response of allogeneic PBMC

To examine the immunomodulatory capacity of cATMSC-EV embedded in cardiac scaffolds, we studied the cytokine response of allogeneic PBMC, stimulated or not with PMA plus Io, and cultured with cardiac scaffolds filled with hydrogel alone or mixed with cATMSC-EV. The presence of the scaffolds themselves already weakened cytokine secretion by stimulated PBMC (Fig. S7), which could be attributed to

both biological effects or to technical reasons, as scaffolds would be greatly hindering PBMC cell contact. There were only a few exceptions: IL6 and IL8 were secreted by stimulated PBMC in the presence of myocardial scaffolds, which was increased with cATMSC-EV, while very low levels of IFNγ and TNFα were found. Notably, only IL6 secretion was found in the presence of cATMSC-EV embedded in pericardial scaffolds, whereas none of the other pro-inflammatory cytokines were detected. Therefore, pericardial scaffold was the preferred construct to be tested *in vivo* due to its improved EV retention and low immunoreactivity.

3.7. Locally administered porcine cATMSC-EV stay within scaffolds and infarct core

To assess safety and biodistribution of the cATMSC-EV once administered *in vivo*, a study was performed using the acute MI pig model. Pericardial scaffolds containing NIR815-labelled cATMSC-EV mixed in peptide hydrogel were implanted over the ischemic area of treated animals, and were compared to the use of a hydrogel-alone filled scaffold in control animals. Fluorescent signal of scaffolds loaded with NIR815-cATMSC-EV was confirmed before implantation (Fig. S8). One animal died after ventricular fibrillation during MI induction and one exhibited no evidence of MI and was excluded from the final analysis, which included three treated and three control animals. Six days after implantation, porcine hearts and sections, as detailed in (Fig. S9), were scanned to track the presence of NIR815-labelled cATMSC-EV. They were detected in both the graft and infarct core, and had persisted only within the damaged area of treated animals (Fig. 6 and Fig. S10).

3.8. In vivo scaffold neovascularization and reduction of macrophage and T cell infiltration

All the scaffolds integrated to the myocardium, showing neo-innervation and neovascularization regardless of EV loading (Fig. S11) as previously observed [13]. Nevertheless, cATMSC-EV presence induced greater vascular density within scaffolds (Fig. 7A–B; 0.15%

(0.058) *vs* 0.93% (0.410) IsoB4 area in Control *vs* Treated animals; $p = 0.031$). Regarding the MI area, although not significant, less fibrotic area was observed in the infarct core (Fig. 7C; 0.46% (0.35) *vs* 0.13% (0.06) Collagen I area in Control *vs* Treated animals; $p = 0.2$). Moreover, treated animals had a marked decrease of infiltrating monocytes (CD163+) in the infarct core (Fig. 7D–E) (26.38% (2.3) *vs* 1.942% (2.91) in Control *vs* Treated animals; $p = 0.002$), whereas no differences were found within the scaffold itself (32.7% (9.26) *vs* 30.08% (12.60); $p = 0.78$). Regarding B cell infiltration, it was rare and no differences were found (Fig. 7F–G). On the other hand, the decrease in macrophages was accompanied with a reduction in T cell infiltration, observed in the infarcted tissue (Fig. 7F–G) (27.23% (7.86) *vs* 11.66% (0.97) in Control *vs* Treated animals; $p = 0.008$), but not significant in the scaffold area (22.61% (12.78) *vs* 16.66% (4.59) in Control *vs* Treated animals; $p = 0.53$). No significant differences were found either in the amount of CD25+ T cells.

4. Discussion

In the present study, we deepen into the beneficial properties of porcine MSC-EV isolated by SEC for reparative medicine, set up potential immunomodulatory, chemotactic and pro-angiogenic potency assays and unravel a new role of porcine MSC-EV as recruiters of endogenous pro-angiogenic cells. At the same time, we describe the development of a new generation of cell-free cardiac grafts comprising MSC-derived EV embedded with peptide hydrogels in cardiac decellularised scaffolds for local myocardial delivery.

Cardiac tissue engineering, which is based on the scaffolding of reparative cells and/or bioactive factors with supportive materials, is a potential alternative therapy to limit adverse ventricular remodelling, and ultimately preserve heart function post-MI [31]. In this context, decellularised cardiac scaffolds are a source of biological ECM derived from native cardiac tissues, with conserved micro- and macro-scale ECM structure and functional cardiac ECM composition [32,33]. Specifically, we already have a protocol approved by the Spanish Agency of
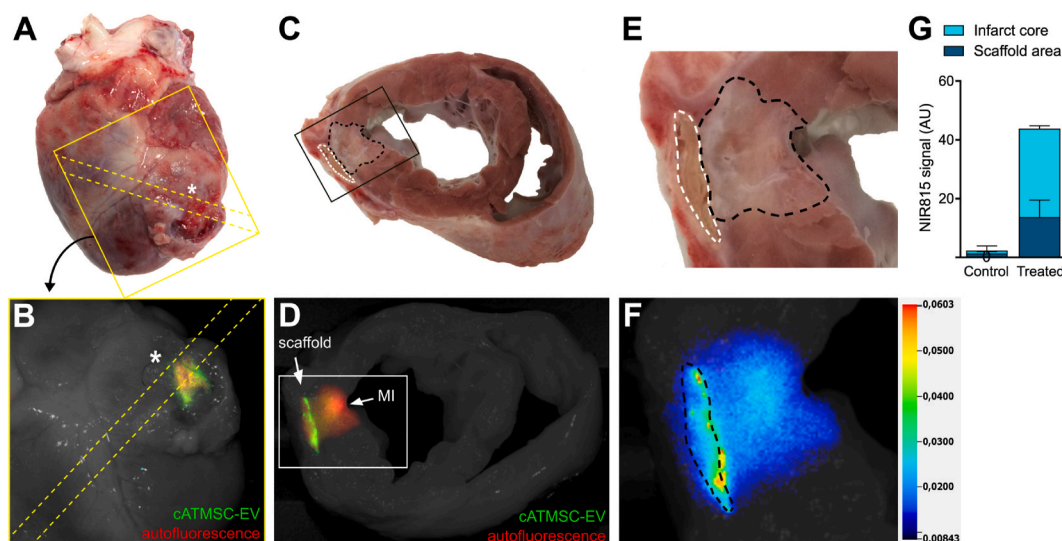
Fig. 6. Porcine NIR815-cATMSC-EV detection in the scaffold and infarct area *in vivo* after six days post-implantation. Representative images of one treated animal are shown. **(A, B)** Anterior side of a treated pig heart six days after MI. Heart sectioning is indicated by yellow dotted line. **(A)** The scaffold (not visible due to the tissue coverage) was implanted following the coronary branch descending from the MI ligation (*). **(B)** Fluorescent scanning and bright field photography of the region of the heart indicated in **(A)**. The NIR815-EV fluorescence (green; 800 nm) could be detected through, and despite the covering tissue, where the scaffold was implanted. **(C)** The scaffold (white dotted line) and MI area (black dotted line) can be observed in the transversal cut of the 1.5 cm-heart section spanning from the MI ligation to the half of the scaffold. **(D)** Administered NIR815-cATMSC-EV (green; 800 nm) are detected within the scaffold and MI core (red; autofluorescence; 700 nm) by fluorescent tracking. Both fluorescent signals are overlaid on a white light image of the heart section. **(E)** Close-up image of the scaffold (white dotted line) and MI area (black dotted line). **(F)** Pseudo-colour intensity image depicting NIR815-EV signal at the 800 nm channel within the scaffold (black dotted line) and infarct core. **(G)** Quantification of NIR815 signal in the infarct and scaffold area. Bars indicate mean ± SD. $p < 0.001$ difference in the infarct core and $p < 0.01$ in the scaffold area between Control (n = 3) and Treated animals (n = 3) by Two-way ANOVA.
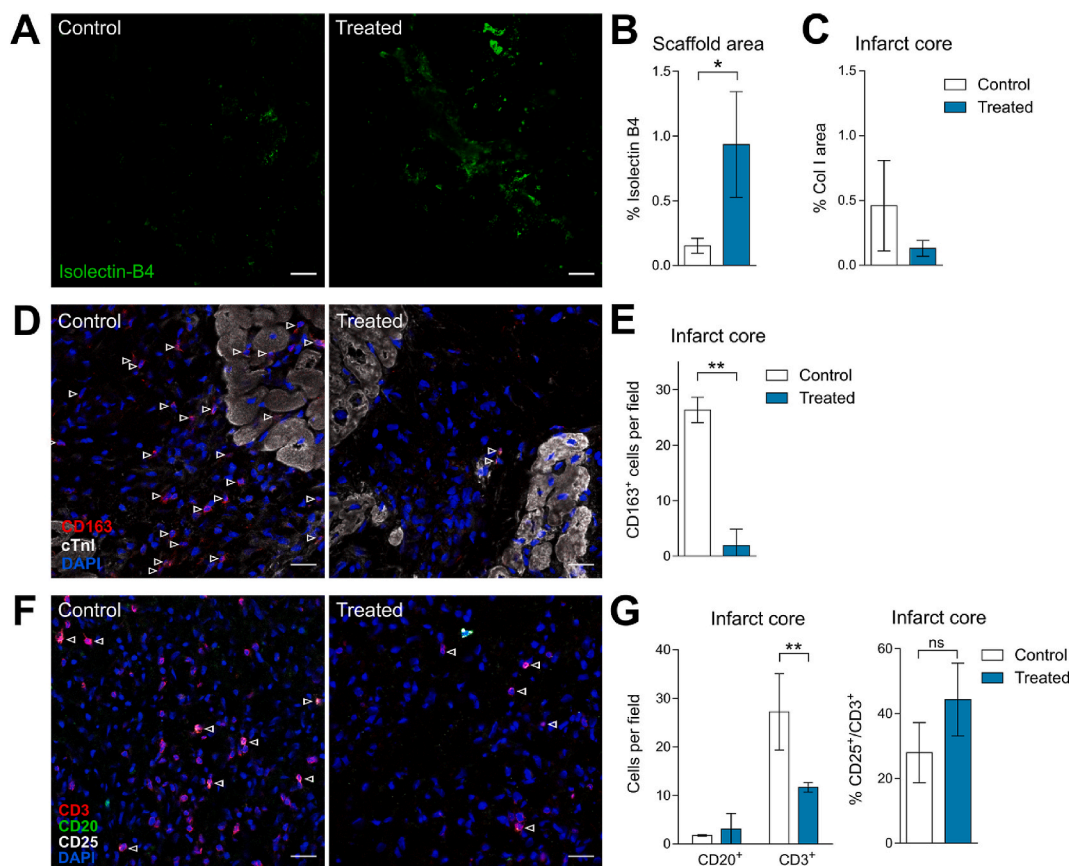
Fig. 7. Porcine cATMSC-EV induce more neovascularization within the scaffold and less infiltrating macrophages in the infarct area. **(A)** Representative images of scaffold areas from a Control and Treated animals stained with Isolectin-B4 (green) showed an increase in vascular density when cATMSC-EV were loaded to the scaffolds. **(B)** Percentage of vessel area within the scaffold. **(C)** Percentage of collagen I area within the infarct area, assessed by Sirius Red staining. **(D)** Immunohistofluorescence against CD163 (red), cTnI (white), and DAPI (blue) of Control and Treated animals of the infarct core show a reduced macrophage infiltration when cATMSC-EV were implanted with scaffolds. Arrows indicate macrophages (CD163$^+$) found within the infarct core. **(E)** The number of CD163$^+$ cells per field within the infarct core. *$p < 0.05$; **$p < 0.01$ by T-Student test. **(F)** Immunohistofluorescence against CD3 (red), CD25 (white), CD20 (green) and DAPI (blue) of Control and Treated animals of the infarct core show a reduced T cell infiltration when cATMSC-EV were implanted with scaffolds. Arrows indicate activated T cells (CD3$^+$CD25$^+$). **(G)** The number of infiltrating B cells (CD20$^+$) and T cells (CD3$^+$) per field and % of CD25$^+$ T cells (CD3$^+$) per field within the infarct core. Bars indicate mean ± SD corresponding to three animals per group. **$p < 0.01$ by Two-way ANOVA. Scale bar = 20 μm.

Medicines and Medical Devices (AEMPS; PEI18-140) to produce clinical-grade scaffolds from healthy pericardium of cadaveric donors, and currently being used in a clinical trial [34].

Following our established decellularisation methods, we obtain acellular cardiac constructs that can be rehydrated with aqueous peptide hydrogels, and repopulated with cATMSC [7,12,26] or presently, EV. In our previous studies, the implantation of scaffolds with cATMSC improved post-MI cardiac function in the preclinical swine model. Microscopically, the engineered grafts integrated with the underlying myocardium, and showed signs of neoinnervation and neovascularization [10–13]. However, despite exhibiting promising results, it remains uncertain how the implanted cells contribute to MI recovery, since, as many others also report, administered cells display poor survival and engraftment, and negligible proliferation and differentiation within the myocardial tissue. A plausible hypothesis would be that instead of replacing the injured tissue themselves, cATMSC would reduce the ischemic injury-triggered inflammation by modulating the host's immune system and foster endogenous regeneration in a paracrine fashion. Specifically, they induce CD73 expression in M2-like polarised monocytes and reduce the number of activated CD4$^+$CD25$^+$ T cells [11,35], along with recruiting peripheral progenitor cells via trophic factors [15,36–39]. Based on our previous findings and the increasing evidence that EV play important roles in MSC's paracrine effects [17,18,40], we decided to design and study a new generation of

cell-free cardiac grafts, based on the potential of cATMSC-EV combined with our tissue engineering approach. Rationally, EV have several advantages over cells thanks to their unchanged phenotype, lack of tumorigenicity, limited immunoreactivity, and better biodistribution and stability. In fact, the sustained delivery of distinct EV sources using a variety of injectable hydrogels or engineered patches is currently under scrutiny [41–43]. To this end, we purified porcine cATMSC-EV by SEC, a stringent method that yields a pool of MSC-derived EV already proven to be immunomodulatory when derived from human samples [18].

In the present work, we show that porcine cATMSC-EV inhibit polyclonal activation (proliferation and pro-inflammatory cytokine production) of allogeneic immune cells, comparable to post-MI circumstances. Following the ischemic injury, danger-associated signals released by cardiomyocyte death and ECM degradation trigger an inflammatory reaction, including the production of inflammatory cytokines (IL1β, IFNγ, TNFα and IL6) and chemokines that activate and recruit the innate immune system. While this initial response is crucial for dead cell clearance and tissue repair, its timely repression would prevent detrimental inflammation and amplification of the myocardial damage [44,45].

Here we report that cATMSC-EV abrogated the secretion of TNFα, a cytokine extensively associated to cardiac damage and worsening of heart failure symptoms [44]. On the other hand, IL6 and IL8 levels were unaltered by porcine cATMSC-EV. While IL6 production has

controversial functions in MI, it has been also related to the initiation of reparative processes [46–49]. As to IL8, it recruits the neutrophils needed after MI for clearance of dead cells and degraded ECM, and assisting the initiation of the inflammatory phase. However, neutrophil ablation does not correlate to a change in infarct size [48].

Regarding IFNγ and IL12, available *in vivo* data report Th1-polarized CD4$^+$ T cells the predominantly present in the ischemic myocardium [50]. Moreover, experiments in RAG1 KO mice reconstituted with CD4$^+$ T cells from either WT or IFNγ-KO mice beautifully uncovered that IFNγ-mediated Th1 CD4$^+$ T cells contribute to MI injury [51,52]. Thus, it is encouraging that cATMSC-EV suppress the production of IFNγ and the Th1-driving IL12, translating in a decrease on T cell infiltration *in vivo*. Finally, the known interferon- and IL12-dependent IL10 production might explain its concomitant reduction in our experiments [53,54]. Moreover, there could be other immunoregulatory mediators playing a role besides IL10 that have not been studied. In summary, the decrease in pro-inflammatory cytokines evidences the powerful immune modulatory effect of cATMSC-EV towards allogeneic polyclonal activation.

The exploratory *in vitro* experiments incorporating scaffolds to stimulated PBMC proved difficult to interpret, as the mere presence of the unloaded scaffolds already disrupted cytokine production, likely due to minimized cell interaction. Unexpectedly, cATMSC-EV addition to either type of scaffold spiked IL6 production. Although we do not have a clear explanation for this phenomenon, and we cannot affirm whether this also happens *in vivo*, it did not translate into an adverse reaction after *in vivo* scaffold implantation. Individually, only cATMSC-EV combined with myocardial scaffolds increased IFNγ, TNFα, and IL8, although still in less amounts than stimulated PBMC alone. On the other hand, and despite being of human origin, pericardial scaffolds did not induce such cytokine response, suggesting absence of xenoreactivity. Moreover, pericardial scaffolds seemed to retain multifunctional cATMSC-EV in a larger extent in comparison with myocardial scaffolds. Along this line, the bigger caveats of pericardial scaffolds already displayed better cell penetrance and retention. Other differences regarding EV or immune interaction could be explained by the different biochemical composition, variations in signalling ligands between the two scaffolds [12]. These findings support our downstream proof-of-concept *in vivo* experiments combining cATMSC-EV with pericardial scaffolds.

This EV delivery strategy aims at magnifying the local effective dose of administered EV, thus downsizing the required EV units and side targets. In fact, fluorescence-aided tracking of EV showed the confinement and slow release of EV within scaffolds, even once implanted. Interestingly, fluorescent signal could be also found within the infarct core, indicating that either cATMSC-EV were present there, or that cells that interacted with EV -and therefore acquired the dye-were later on migrating towards the MI area. Also, the combination of EV with tissue engineering, such as injectable ECM hydrogels, allows a prolonged release of its embedded EV instead of rapid diffusion, and protect EV from degradation [42,43,55].

cATMSC-EV showed immune suppressive properties and, for the first time to our knowledge, we provide evidence of MSC-EV-mediated directed recruitment of allogeneic pro-regenerative cells, including allogeneic MSC and peripheral blood-derived OEC *in vitro*. This concurred with angiogenesis promotion *in vitro* and translated to an enhanced on-site neovasculogenesis *in vivo*, an essential first step to trigger endogenous cardiac repair. The power of EV-mediated recruitment was shown by De la Fuente and colleagues, using tumour-derived EV as bait to successfully attract and encapsulate circulating metastatic cells to an artificial 3D scaffold and enable their localised surgical removal [56]. In addition, EV can bear functional chemokines attached to surface [57], enabling recognition by cells. Ahmed and colleagues demonstrated that a concentration gradient is established across and within the agarose spot (in their case, purified chemokines), leading to cell recruitment towards the centre of the spot of cells in close contact with the spot, while cells in a remote position have a stochastic movement and do not respond to the chemokines stimuli [24]. In line, our experiments indicate that cells are indeed sensing chemoattractant molecules present in EV, as only the OEC and MSC in contact with cATMSC-EV were attracted towards them.

On the other side, the administration of cATMSC-EV greatly reduced the number of infiltrating monocytes and T cells in the MI core six days after MI induction, which would correlate with the anti-inflammatory properties of cATMSC-EV observed *in vitro*. Within this relatively short time span monocytes are known to be found in great numbers in the post-ischemic myocardium, and recent studies suggest that infiltrating monocytes are responsible of exacerbating the inflammatory milieu post-MI that further deteriorates myocardial tissue [58–60]. Notably, although the percentage of CD25$^+$ T cells was unchanged, the overall number of T cells within the damaged MI tissue decreased. Thus, this marked change in infiltrating immune cells induced by MSC-EV could be indicative of the promotion of a shift from the inflammatory towards a regenerative phase, something that merits further investigation in longer time points. Of note, infiltration within the scaffold was low and did not change with cATMSC-EV, indicating the lack of immune reactivity.

Finally, with clinical translation in mind, it would be interesting to study the bioequivalence of cATMSC-EV and EV derived from other sources of human MSC-EV, such as umbilical cord, with better availability, less ethical concerns and less epigenetic/environmental imprinting than adult sources of MSCs.

In summary, our data support the potential of multifunctional cATMSC-EV combined with biocompatible cardiac scaffolds generated by decellularisation of human pericardium for effective local delivery over post-infarcted myocardial tissue. Moreover, SEC is a valuable method to obtain highly purified MSC-EV with functional properties reciprocal to their parental MSC [18,61]. Noticeably, we find MSC-EV to be anti-inflammatory, as well as able to recruit pro-regenerative cells and promote angiogenesis *in vivo*. Hence, MSC-EV delivery into post-infarcted myocardium presumably generates a highly bioactive niche that triggers endogeneous cardiac repair. Nonetheless, further studies are mandatory to corroborate the effectiveness of this cell-free tissue engineering approach to benefit cardiac healing and ultimately improve cardiac function in the long-term.

Funding sources

CRediT authorship contribution statement

Marta Monguió-Tortajada: designed the study, performed experiments, Formal analysis, Data curation, Writing – original draft, Writing – review & editing. **Cristina Prat-Vidal:** performed experiments, Formal analysis, Data curation, Writing – original draft, Writing – review & editing. **Miriam Moron-Font:** performed experiments, Writing – review & editing. **Marta Clos-Sansalvador:** performed experiments, Writing – review & editing. **Alexandra Calle:** performed experiments, Writing – review & editing. **Paloma Gastelurrutia:** performed experiments, Writing – review & editing. **Adriana Cserkoova:** performed experiments, Writing – review & editing. **Anna Morancho:** performed experiments, Writing – review & editing. **Miguel Ángel Ramírez:** conceptual advice, Writing – original draft, Writing – review & editing. **Anna Rosell:** conceptual advice, Writing – original draft, Writing – review & editing. **Antoni Bayes-Genis:** conceptual advice, Writing – original draft, Writing – review & editing. **Carolina Gálvez-Montón:** designed the study, performed experiments, Formal analysis, Data curation, Writing – original draft, Writing – review & editing. **Francesc E. Borràs:** designed the study, Formal analysis, Data curation, Writing – original draft, Writing – review & editing. **Santiago Roura:** designed the study, performed experiments, Formal analysis, Data curation, Writing – original draft, Writing – review & editing.

Declaration of competing interest

The authors declare that they have no known competing financial interests or personal relationships that could have appeared to influence the work reported in this paper.

Acknowledgements

Abbreviations

BSA	bovine serum albumin
cATMSC	cardiac adipose tissue-derived MSC
CCM	concentrated conditioned medium
cryo-EM	cryo-electron microscopy
DAPI	4′,6-diamidino-2-phenylindole
EBM-2	endothelial cell basal medium-2
ECM	extracellular matrix
EGM-2	endothelial growth medium-2
EV	extracellular vesicles
FBS	foetal bovine serum
hEGF	human endothelial growth factor
hFGF-B	human basic fibroblast growth factor
IM	intramuscular
Io	ionomycin
IV	intravenous
MFI	median fluorescence intensity
MI	myocardial infarction
MSC	mesenchymal stromal cell
OEC	outgrowth endothelial cell
PBS	phosphate-buffered saline
PBMC	peripheral blood mononuclear cells

PMA	phorbol 12-myristate 13-acetate
P/S	penicillin-streptomycin
RT	room temperature
SEC	size exclusion chromatography
SEM	scanning electron microscopy
3D	three-dimensional
TBS	tris-buffered saline
T-PBS	Tween-PBS
UC	ultracentrifugation
VEGF	vascular endothelial growth factor

Appendix A. Supplementary data

Supplementary data to this article can be found online at https://doi.org/10.1016/j.bioactmat.2021.02.026.

References

[1] World Health Organization, Global Health Estimates 2016: Deaths by Cause, Age, Sex, by Country and by Region, 2000-2016, 2018.

[2] G. Olivetti, J.M. Capasso, L.G. Meggs, et al., Cellular basis of chronic ventricular remodeling after myocardial infarction in rats, Circ. Res. 68 (1991) 856–869, https://doi.org/10.1161/01.RES.68.3.856.

[3] M. Metra, P. Ponikowski, K. Dickstein, et al., Advanced chronic heart failure: a position statement from the study group on advanced heart failure of the heart failure association of the European society of cardiology, Eur. J. Heart Fail. 9 (2007) 684–694.

[4] M.C. Alraies, P. Eckman, Adult heart transplant: indications and outcomes, J. Thorac. Dis. 6 (2014) 1120–1128, https://doi.org/10.3978/j.issn.2072-1439.2014.06.44.

[5] M.W. Curtis, B. Russell, Cardiac tissue engineering, J. Cardiovasc. Nurs. 24 (2009) 87–92, https://doi.org/10.1097/01.JCN.0000343562.06614.49.

[6] A. Bayes-Genis, C. Soler-Botija, J. Farré, et al., Human progenitor cells derived from cardiac adipose tissue ameliorate myocardial infarction in rodents, J. Mol. Cell. Cardiol. 49 (2010), https://doi.org/10.1016/j.yjmcc.2010.08.010.

[7] C. Prat-Vidal, C. Gálvez-Montón, V. Puig-Sanvicens, et al., Online monitoring of myocardial bioprosthesis for cardiac repair, Int. J. Cardiol. 174 (2014) 654–661, https://doi.org/10.1016/j.ijcard.2014.04.181.

[8] S. Roura, C. Soler-Botija, J.R. Bagó, et al., Postinfarction functional recovery driven by a three-dimensional engineered fibrin patch composed of human umbilical cord blood-derived mesenchymal stem cells, Stem Cells Transl. Med 4 (2015) 956–966, https://doi.org/10.5966/sctm.2014-0259.

[9] L. Bagno, K.E. Hatzistergos, W. Balkan, J.M. Hare, Mesenchymal stem cell-based therapy for cardiovascular disease: progress and challenges, Mol. Ther. 26 (2018) 1610–1623, https://doi.org/10.1016/J.YMTHE.2018.05.009.

[10] I. Perea-Gil, C. Prat-Vidal, C. Gálvez-Montón, et al., A cell-enriched engineered myocardial graft limits infarct size and improves cardiac function: pre-clinical study in the porcine myocardial infarction model, JACC Basic Transl. Sci. 1 (2016) 360–372, https://doi.org/10.1016/j.jacbts.2016.06.005.

[11] C. Gálvez-Montón, R. Bragós, C. Soler-Botija, et al., Noninvasive assessment of an engineered bioactive graft in myocardial infarction: impact on cardiac function and scar healing, Stem Cells Transl. Med. 6 (2017) 647–655, https://doi.org/10.5966/sctm.2016-0063.

[12] I. Perea-Gil, C. Gálvez-Montón, C. Prat-Vidal, et al., Head-to-head comparison of two engineered cardiac grafts for myocardial repair : from scaffold characterization to pre-clinical testing, Sci. Rep. 8 (2018) 1–13, https://doi.org/10.1038/s41598-018-25115-2, 6708.

[13] C. Gálvez-Montón, M.T. Fernandez-Figueras, M. Martí, et al., Neoinnervation and neovascularization of acellular pericardial-derived scaffolds in myocardial infarcts, Stem Cell Res. Ther. 6 (2015) 108, https://doi.org/10.1186/s13287-015-0101-6.

[14] K.M. Broughton, B.J. Wang, F. Firouzi, et al., Mechanisms of cardiac repair and regeneration, Circ. Res. 122 (2018) 1151–1163, https://doi.org/10.1161/CIRCRESAHA.117.312586.

[15] K. Malliaras, Y. Zhang, J. Seinfeld, et al., Cardiomyocyte proliferation and progenitor cell recruitment underlie therapeutic regeneration after myocardial infarction in the adult mouse heart, EMBO Mol. Med. 5 (2013) 191–209, https://doi.org/10.1002/emmm.201201737.

[16] A.I. Caplan, Mesenchymal stem cells: time to change the name!, Stem Cells Transl. Med. 6 (2017) 1445–1451, https://doi.org/10.1002/sctm.17-0051.

[17] M. Yáñez-Mó, P.R.-M. Siljander, Z. Andreu, et al., Biological properties of extracellular vesicles and their physiological functions, J. Extracell. Vesicles 4 (2015) 27066, https://doi.org/10.3402/jev.v4.27066.

[18] M. Monguió-Tortajada, S. Roura, C. Gálvez-Montón, et al., Nanosized UCMSC-derived extracellular vesicles but not conditioned medium exclusively inhibit the inflammatory response of stimulated T cells: implications for nanomedicine, Theranostics 7 (2017) 270–284, https://doi.org/10.7150/thno.16154.

[19] M. Monguió-Tortajada, M. Morón-Font, A. Gámez-Valero, et al., Extracellular-vesicle isolation from different biological fluids by size-exclusion chromatography, Curr. Protoc. Stem Cell Biol. e82 (2019) 1–24, https://doi.org/10.1002/cpsc.82.

[20] J. Van Deun, P. Mestdagh, P. Agostinis, et al., EV-TRACK: transparent reporting and centralizing knowledge in extracellular vesicle research, Nat. Methods 14 (2017) 228–232, https://doi.org/10.1038/nmeth.4185.

[21] A. Gámez-Valero, M. Monguió-Tortajada, L. Carreras-Planella, et al., Size-Exclusion Chromatography-based isolation minimally alters Extracellular Vesicles' characteristics compared to precipitating agents, Sci. Rep. 6 (2016) 33641, https://doi.org/10.1038/srep33641.

[22] I. Lozano-Ramos, I. Bancu, A. Oliveira-Tercero, et al., Size-exclusion chromatography-based enrichment of extracellular vesicles from urine samples, J. Extracell. Vesicles 4 (2015) 27369, https://doi.org/10.3402/jev.v4.27369.

[23] M. Navarro-Sobrino, A. Rosell, M. Hernandez-Guillamon, et al., Mobilization, endothelial differentiation and functional capacity of endothelial progenitor cells after ischemic stroke, Microvasc. Res. 80 (2010) 317–323, https://doi.org/10.1016/j.mvr.2010.05.008.

[24] M. Ahmed, H.A. Basheer, J.M. Ayuso, et al., Agarose spot as a comparative method for in situ analysis of simultaneous chemotactic responses to multiple chemokines, Sci. Rep. 7 (2017) 1–11, https://doi.org/10.1038/s41598-017-00949-4.

[25] A. Calle, C. Barrajón-Masa, E. Gómez-Fidalgo, et al., Iberian pig mesenchymal stem/stromal cells from dermal skin, abdominal and subcutaneous adipose tissues, and peripheral blood: in vitro characterization and migratory properties in inflammation, Stem Cell Res. Ther. 9 (2018) 178, https://doi.org/10.1186/s13287-018-0933-y.

[26] I. Perea-Gil, J.J. Uriarte, C. Prat-Vidal, et al., In vitro comparative study of two decellularization protocols in search of an optimal myocardial scaffold for recellularization, Am. J. Transl. Res. 7 (2015) 558–573.

[27] NIH, Guide for the Care and Use of Laboratory Animals, eighth ed., National Academies Press, Washington, D.C, 2011.

[28] C. Gálvez-Montón, C. Prat-Vidal, S. Roura, et al., Transposition of a pericardial-derived vascular adipose flap for myocardial salvage after infarct, Cardiovasc. Res. 91 (2011) 659–667, https://doi.org/10.1093/cvr/cvr136.

[29] L. Kordelas, V. Rebmann, A.K. Ludwig, et al., MSC-derived exosomes: a novel tool to treat therapy-refractory graft-versus-host disease, Leukemia 28 (2014) 970–973.

[30] M. Tkach, J. Kowal, A.E. Zucchetti, et al., Qualitative differences in T-cell activation by dendritic cell-derived extracellular vesicle subtypes, EMBO J. 36 (2017) 3012–3028, https://doi.org/10.15252/embj.201696003.

[31] C. Gálvez-Montón, C. Prat-Vidal, S. Roura, et al., Update: innovation in cardiology (IV). Cardiac tissue engineering and the bioartificial heart, Rev. Esp. Cardiol. 66 (2013) 391–399, https://doi.org/10.1016/j.rec.2012.11.012.

[32] P.M. Crapo, T.W. Gilbert, S.F. Badylak, An overview of tissue and whole organ decellularization processes, Biomaterials 32 (2011) 3233–3243, https://doi.org/10.1016/j.biomaterials.2011.01.057.

[33] D.A. Taylor, L.C. Sampaio, Z. Ferdous, et al., Decellularized matrices in regenerative medicine, Acta Biomater. (2018), https://doi.org/10.1016/j.actbio.2018.04.044.

[34] C. Prat-Vidal, L. Rodríguez-Gómez, M. Aylagas, et al., First-in-human PeriCord cardiac bioimplant: scalability and GMP manufacturing of an allogeneic engineered tissue graft, EBioMedicine 54 (2020) 102729, https://doi.org/10.1016/j.ebiom.2020.102729.

[35] M. Monguió-Tortajada, S. Roura, C. Gálvez-Montón, et al., Mesenchymal stem cells induce expression of CD73 in human monocytes in vitro and in a swine model of myocardial infarction in vivo, Front. Immunol. 8 (2017) 1577, https://doi.org/10.3389/fimmu.2017.01577.

[36] R.H. Lee, A.A. Pulin, M.J. Seo, et al., Intravenous hMSCs improve myocardial infarction in mice because cells embolized in lung are activated to secrete the anti-inflammatory protein TSG-6, Cell Stem Cell 5 (2009) 54–63, https://doi.org/10.1016/j.stem.2009.05.003.

[37] E. Eggenhofer, V. Benseler, A. Kroemer, et al., Mesenchymal stem cells are short-lived and do not migrate beyond the lungs after intravenous infusion, Front. Immunol. 3 (2012) 297, https://doi.org/10.3389/fimmu.2012.00297.

[38] K. Le Blanc, D. Mougiakakos, Multipotent mesenchymal stromal cells and the innate immune system, Nat. Rev. Immunol. 12 (2012) 383–396, https://doi.org/10.1038/nri3209.

[39] T. Ben-Mordechai, R. Holbova, N. Landa-Rouben, et al., Macrophage subpopulations are essential for infarct repair with and without stem cell therapy, J. Am. Coll. Cardiol. 62 (2013) 1890–1901, https://doi.org/10.1016/j.jacc.2013.07.057.

[40] L. Timmers, S.K. Lim, F. Arslan, et al., Reduction of myocardial infarct size by human mesenchymal stem cell conditioned medium, Stem Cell Res. 1 (2008) 129–137, https://doi.org/10.1016/J.SCR.2008.02.002.

[41] J.J. Chung, J. Han, L.L. Wang, et al., Delayed delivery of endothelial progenitor cell-derived extracellular vesicles via shear thinning gel improves postinfarct hemodynamics, J. Thorac Cardiovasc. Surg. (2019), https://doi.org/10.1016/j.jtcvs.2019.06.017.

[42] C. Han, J. Zhou, C. Liang, et al., Human umbilical cord mesenchymal stem cell derived exosomes encapsulated in functional peptide hydrogels promote cardiac repair, Biomater. Sci. 7 (2019) 2920–2933, https://doi.org/10.1039/C9BM00101H.

[43] B. Liu, B.W. Lee, K. Nakanishi, et al., Cardiac recovery via extended cell-free delivery of extracellular vesicles secreted by cardiomyocytes derived from induced pluripotent stem cells, Nat. Biomed. Eng. 2 (2018) 293–303, https://doi.org/10.1038/s41551-018-0229-7.

[44] S. Frantz, J. Bauersachs, R.A. Kelly, Innate immunity and the heart, Curr. Pharmaceut. Des. 11 (2005) 1279–1290.

[45] N.G. Frangogiannis, The inflammatory response in myocardial injury, repair and remodelling, Nat. Rev. Cardiol. 11 (2014) 255–265, https://doi.org/10.1038/nrcardio.2014.28.

[46] B. Dawn, Y.T. Xuan, Y. Guo, et al., IL-6 plays an obligatory role in late preconditioning via JAK-STAT signaling and upregulation of iNOS and COX-2, Cardiovasc. Res. 64 (2004) 61–71, https://doi.org/10.1016/j.cardiores.2004.05.011.

[47] N. Smart, M.H. Mojet, D.S. Latchman, et al., IL-6 induces PI 3-kinase and nitric oxide-dependent protection and preserves mitochondrial function in cardiomyocytes, Cardiovasc. Res. 69 (2006) 164–177, https://doi.org/10.1016/j.cardiores.2005.08.017.

[48] N.G. Frangogiannis, The immune system and the remodeling infarcted heart: cell biological insights and therapeutic opportunities, J. Cardiovasc. Pharmacol. 63 (2014) 185–195, https://doi.org/10.1097/FJC.0000000000000003. The.

[49] A.E. Mayfield, P. Kanda, A. Nantsios, et al., Interleukin-6 mediates post-infarct repair by cardiac explant-derived stem cells, Theranostics 7 (2017) 4850–4861, https://doi.org/10.7150/thno.19435.

[50] U. Hofmann, S. Frantz, Role of lymphocytes in myocardial injury, healing, and remodeling after myocardial infarction, Circ. Res. 116 (2015) 354–367, https://doi.org/10.1161/CIRCRESAHA.116.304072.

[51] Z. Yang, Y.-J. Day, M.-C. Toufektsian, et al., Myocardial infarct-sparing effect of adenosine A2A receptor activation is due to its action on CD4+ T lymphocytes, Circulation 114 (2006) 2056–2064, https://doi.org/10.1161/CIRCULATIONAHA.106.649244.

[52] S.E. Boag, E. Andreano, I. Spyridopoulos, Lymphocyte communication in myocardial ischemia/reperfusion injury, Antioxidants Redox Signal. 26 (2016) 6940, https://doi.org/10.1089/ars.2016.6940, ars.2016.

[53] S. Rutz, W. Ouyang, Regulation of interleukin-10 and interleukin-22 expression in T helper cells, Curr. Opin. Immunol. 23 (2011) 605–612, https://doi.org/10.1016/J.COI.2011.07.018.

[54] C.A. Stewart, H. Metheny, N. Iida, et al., Interferon-dependent IL-10 production by Tregs limits tumor Th17 inflammation, J. Clin. Invest. 123 (2013) 4859–4874, https://doi.org/10.1172/JCI65180.

[55] M.J. Hernandez, K.L. Christman, Designing acellular injectable biomaterial therapeutics for treating myocardial infarction and peripheral artery disease, JACC Basic Transl. Sci. 2 (2017) 212–226, https://doi.org/10.1016/J.JACBTS.2016.11.008.

[56] A. de la Fuente, L. Alonso-Alconada, C. Costa, et al., M-trap: exosome-based capture of tumor cells as a new technology in peritoneal metastasis, J. Natl. Cancer Inst. 107 (2015) djv184, https://doi.org/10.1093/jnci/djv184.

[57] J. Berenguer, T. Lagerweij, X.W. Zhao, et al., Glycosylated extracellular vesicles released by glioblastoma cells are decorated by CCL18 allowing for cellular uptake via chemokine receptor CCR8, J. Extracell. Vesicles 7 (2018) 1446660, https://doi.org/10.1080/20013078.2018.1446660.

[58] Y. Maekawa, T. Anzai, T. Yoshikawa, et al., Prognostic significance of peripheral monocytosis after reperfused acute myocardial infarction:a possible role for left ventricular remodeling, J. Am. Coll. Cardiol. 39 (2002) 241–246, https://doi.org/10.1016/s0735-1097(01)01721-1.

[59] G. Zhao, S. Wang, Z. Wang, et al., CXCR6 deficiency ameliorated myocardial ischemia/reperfusion injury by inhibiting infiltration of monocytes and IFN-γ-dependent autophagy, Int. J. Cardiol. 168 (2013) 853–862, https://doi.org/10.1016/j.ijcard.2012.10.022.

[60] A.M. van der Laan, A. Hirsch, L.F.H.J. Robbers, et al., A proinflammatory monocyte response is associated with myocardial injury and impaired functional outcome in patients with ST-segment elevation myocardial infarction, Am. Heart J. 163 (2012) 57–65, https://doi.org/10.1016/j.ahj.2011.09.002, e2.

[61] I. Perea-Gil, M. Monguió-Tortajada, C. Gálvez-Montón, et al., Preclinical evaluation of the immunomodulatory properties of cardiac adipose tissue progenitor cells using umbilical cord blood mesenchymal stem cells: a direct comparative study, BioMed Res. Int. (2015) 439808, https://doi.org/10.1155/2015/439808, 2015.